ACS OMEGA

Article

Cite This: ACS Omega 2019, 4, 7581−7585

http://pubs.acs.org/journal/acsodf

Synthesis and Color Evaluation of Ta^{5+}-Doped Bi_2O_3

Ryohei Oka, Yusuke Shobu, and Toshiyuki Masui*

Center for Research on Green Sustainable Chemistry, Department of Chemistry, Biotechnology, Graduate School of Engineering, Tottori University, 4-101, Koyama-cho Minami, Tottori 680-8552, Japan

ABSTRACT: Ta^{5+}-doped Bi_2O_3 solid solutions, $(Bi_{1-x}Ta_x)_2O_{3+2x}$ ($0 \le x \le 0.20$), were synthesized by a conventional solid-state reaction method. The crystal structure, optical properties, and color of the pigments were characterized. The $(Bi_{1-x}Ta_x)_2O_{3+2x}$ (x = 0, 0.03, 0.04, 0.20) samples were obtained in a single-phase form, and the crystal structure depended on the Ta content; they were monoclinic α-phase (x = 0), tetragonal β-phase (x = 0.03, 0.04), and cubic δ-phase (x = 0.20). Among them, $(Bi_{0.97}Ta_{0.03})_2O_{3.06}$ strongly absorbed visible light at the wavelength shorter than 480 nm and exhibited the most vivid orange color. The redness value (a^*) was comparable to that of commercial orange pigments, and the yellowness value (b^*) was slightly larger. Although it is necessary to improve chemical stability, the $(Bi_{0.97}Ta_{0.03})_2O_{3.06}$ pigment has potential for an environmentally friendly inorganic orange pigment.

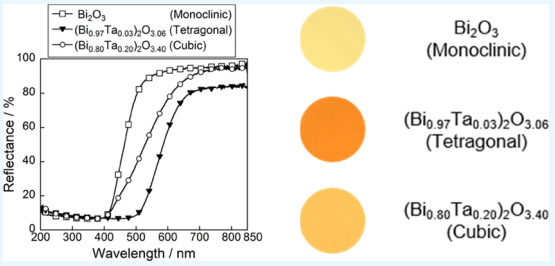

1. INTRODUCTION

Inorganic pigments composed of metal oxides are applied in a broad range of fields, such as ceramics, glasses, plastics, and paints, because they have high hiding power, thermal stability, and weather resistance. In the case of inorganic orange pigments, cadmium orange (CdS·CdSe) and molybdate orange ($PbCrO_4$·$PbMoO_4$·$PbSO_4$) were conventionally used. However, application of these orange pigments containing toxic elements, such as Cd, Pb, Cr, has been forbidden or restricted, because they have harmful effects on the human body and the environment. Therefore, development of inorganic orange pigments without toxic elements is required and several studies have been reported.[1−10]

Because of this situation, we focused on bismuth sesquioxide (Bi_2O_3) because it has been confirmed as virtually nontoxic in medical references.[11−13] Bi_2O_3 has several polymorphs, such as α-phase (monoclinic structure), β-phase (tetragonal structure), γ-phase (body-centered cubic structure), and δ-phase (cubic fluorite structure).[14] The band structure of Bi_2O_3 is constituted by a valence band composed of a hybrid Bi 6s and O 2p orbital and a conduction band of Bi 6p.[15−19] A pale yellowish α phase stably exists at room temperature and is stable up to 730 °C. At 730 °C and above, the α phase is transferred to the orange δ phase. δ-Bi_2O_3 has been suggested as a good electrolyte material for solid oxide fuel cells and gas sensors, because this compound is stable at high temperatures and exhibits high oxide ion conductivity.[14,20−24]

When δ-Bi_2O_3 is cooled from a high temperature, a phase transition to the β phase takes place at 650 °C. Also, the metastable γ-Bi_2O_3 is formed below 650 °C on cooling δ-Bi_2O_3. The structure of β-Bi_2O_3 is a fluorite-based structure, but 25% of the oxide anion is regularly deficient.[25] Although the β and δ phases are unstainable at room temperature, they can be stabilized at room temperature when other cations are introduced into the Bi^{3+} site to form solid solutions. In fact, niobium- and tantalum-doped $(Bi_{1-x}M_x)_2O_{3+2x}$ (M = Nb or Ta) solid solutions adopt β phase and δ phase at room temperature, respectively, to exhibit high oxide anion conductivity.[20] Although Nb^{5+}-doped Bi_2O_3 has been reported as an inorganic reddish-yellow pigment,[26] there is no report on the color evaluation of Ta^{5+}-doped Bi_2O_3 as an inorganic pigment.

In this study, therefore, Ta^{5+}-doped Bi_2O_3 solid solutions, $(Bi_{1-x}Ta_x)_2O_{3+2x}$ ($0 \le x \le 0.20$), were synthesized by a conventional solid-state reaction and their color properties were evaluated as environmentally friendly inorganic orange pigments.

2. RESULTS AND DISCUSSION

2.1. X-ray Powder Diffraction (XRD) and Field-Emission-Type Scanning Electron Microscopic (FE-SEM) Image. Figure 1 shows the XRD patterns of the $(Bi_{1-x}Ta_x)_2O_{3+2x}$ ($0 \le x \le 0.20$) samples. The XRD patterns of α-, β-, and δ-Bi_2O_3 from the inorganic crystal structure database are also shown in this figure as references. The crystal structure depended on the Ta content in $(Bi_{1-x}Ta_x)_2O_{3+2x}$ (x = 0, 0.03, 0.04, 0.20); the monoclinic α-Bi_2O_3 structure (x = 0), the tetragonal β-Bi_2O_3 structure (x = 0.03, 0.04), and the cubic δ-Bi_2O_3 structure (x = 0.20) were obtained in a single-phase form, respectively. However, a mixture of multiple phases was observed in the samples with x = 0.02 and 0.10 because the Ta concentration is near the boundary of the phase transition.

The lattice volumes of tetragonal $(Bi_{1-x}Ta_x)_2O_{2+x}$ (x = 0.03 and 0.04) and cubic $(Bi_{0.80}Ta_{0.20})_2O_{3.40}$ were calculated from the XRD angles, and the results are summarized in Table 1. The lattice volumes of the pure (Ta-free) tetragonal β-Bi_2O_3

Received: February 27, 2019
Accepted: April 15, 2019
Published: April 25, 2019

DOI: 10.1021/acsomega.9b00555
ACS Omega 2019, 4, 7581−7585

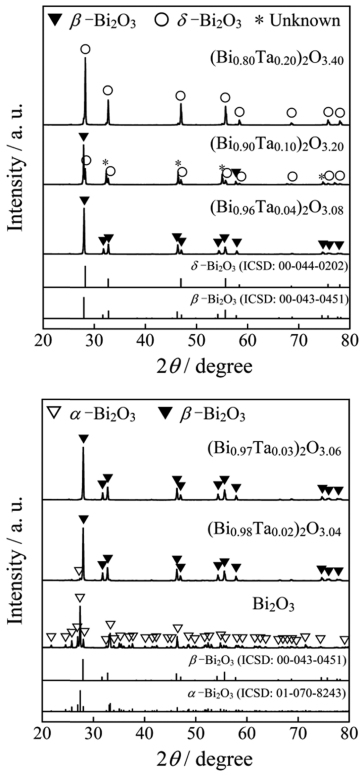

Figure 1. XRD patterns of the $(Bi_{1-x}Ta_x)_2O_{3+2x}$ ($0 \le x \le 0.20$) samples.

Table 1. Lattice Volumes of $(Bi_{1-x}Ta_x)_2O_{3+2x}$ (x = 0.03, 0.04, and 0.20) and Ta-Free Bi_2O_3

composition	crystal system	lattice volume/nm^3
$(Bi_{0.97}Ta_{0.03})_2O_{3.06}$	tetragonal	0.33566(4)
$(Bi_{0.96}Ta_{0.04})_2O_{3.08}$	tetragonal	0.33565(3)
Bi_2O_3[a]	tetragonal	0.33754(3)
$(Bi_{0.80}Ta_{0.20})_2O_{3.40}$	cubic	0.16402(1)
Bi_2O_3[a]	cubic	0.18139(4)

[a]Cited from ref 27.

and cubic δ-Bi_2O_3[27] are also listed as references, where the numbers in parentheses indicate standard deviation. The cell volumes of the tetragonal $(Bi_{0.97}Ta_{0.03})_2O_{3.06}$ and the cubic $(Bi_{0.80}Ta_{0.20})_2O_{3.40}$ samples were smaller than those of the Ta-free tetragonal and cubic Bi_2O_3, respectively. The lattice volumes decreased with increasing the Ta^{5+} content, indicating that Bi^{3+} (ionic radius: 0.103 nm)[28] ions were partially substituted with Ta^{5+} (ionic radius: 0.078 nm)[28] ions. The cell volume of the tetragonal $(Bi_{0.96}Ta_{0.04})_2O_{3.08}$ sample was also smaller than that of the Ta-free tetragonal Bi_2O_3. However, the lattice volume of the tetragonal $(Bi_{0.96}Ta_{0.04})_2O_{3.08}$ and $(Bi_{0.97}Ta_{0.03})_2O_{3.06}$ samples was equal. These results indicate that the solubility limit of Ta^{5+} in the tetragonal β-phase was x = 0.03 for $(Bi_{1-x}Ta_x)_2O_{2+x}$.

Figure 2 shows the FE-SEM images of the $(Bi_{1-x}Ta_x)_2O_{3+2x}$ (x = 0, 0.03, 0.04, and 0.20) samples obtained in a single-phase form. Although aggregated coarse particles were observed in all samples, it was found that only $(Bi_{0.80}Ta_{0.20})_2O_{3.40}$ was composed of small granular particles of about 1 μm somewhat thermally fused.

2.2. Reflectance Spectra. Figure 3 depicts the UV−vis reflectance spectra of the $(Bi_{1-x}Ta_x)_2O_{3+2x}$ (x = 0, 0.03, 0.04, and 0.20) samples obtained in a single-phase form. In all samples, optical absorption was observed by the energy transition from the valence band composed of the hybrid Bi 6s and O 2p orbitals to the conduction band composed of the Bi 6p orbital.[15−18] The tetragonal β-phase samples (x = 0.03 and 0.04) exhibited strong absorption at 480 nm or shorter, whereas the gradual spectral curve was observed for the cubic δ-phase sample (x = 0.20). The absorption wavelengths of the tetragonal $(Bi_{1-x}Ta_x)_2O_{3+2x}$ (x = 0.03 and 0.04) and cubic $(Bi_{0.80}Ta_{0.20})_2O_{3.40}$ samples were obviously observed on the longer wavelength side compared with the monoclinic Bi_2O_3 sample. This behavior was attributed to the fact that the band gap energy of the formers was smaller than that of the latter. The average Bi−O bond distance in each $(Bi_{1-x}Ta_x)_2O_{3+2x}$ (x = 0, 0.03, and 0.20) sample, which was calculated with reference to the literature,[27,29] is summarized in Table 2, where

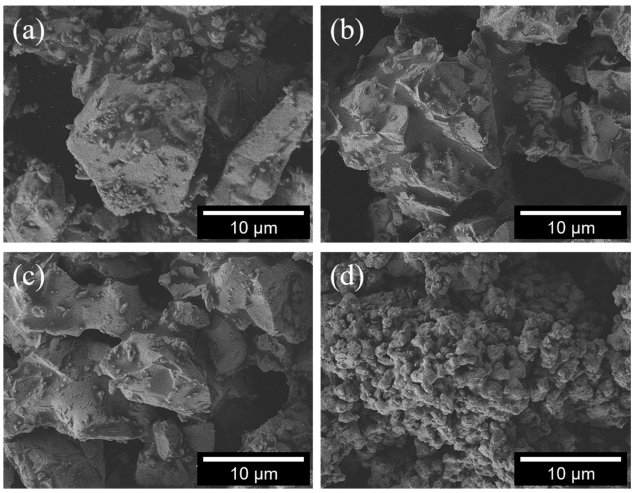

Figure 2. FE-SEM images of the synthesized Bi_2O_3 (a), $(Bi_{0.97}Ta_{0.03})_2O_{3.06}$ (b), $(Bi_{0.96}Ta_{0.04})_2O_{3.08}$ (c), and $(Bi_{0.80}Ta_{0.20})_2O_{3.40}$ (d).

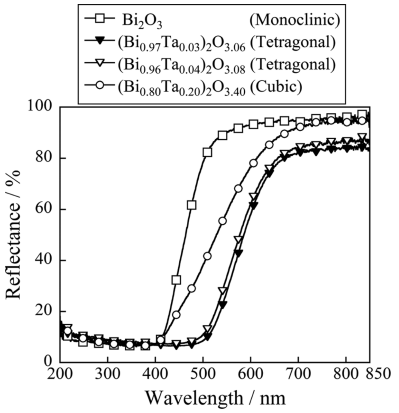

Figure 3. UV−vis reflectance spectra of the $(Bi_{1-x}Ta_x)_2O_{3+2x}$ (x = 0, 0.03, 0.04, and 0.20) samples.

Table 2. Average Bi−O Bond Distance in the $(Bi_{1-x}Ta_x)_2O_{3+2x}$ (x = 0, 0.03, and 0.20) Samples

x	crystal system	average Bi−O bond distance/nm
0	monoclinic	0.24636(3)
0.03	tetragonal	0.23265(4)
0.20	cubic	0.23703(4)

DOI: 10.1021/acsomega.9b00555
ACS Omega 2019, 4, 7581−7585

the numbers in parentheses indicate the standard deviation. The average Bi−O bond length in the crystal lattice was short on the order of the tetragonal $(Bi_{0.97}Ta_{0.03})_2O_{3.06}$, the cubic $(Bi_{0.80}Ta_{0.20})_2O_{3.40}$, and the monoclinic Bi_2O_3 samples. Since the hybrid effect of the Bi 6s and O 2p orbitals in the valence band increases as the Bi−O bond distance decreases,[30,31] the width of the valence band also increases as the Bi−O bond distance becomes shorter. As a result, the band gap energy between the valence and the conduction bands decreases on decreasing the Bi−O bond distance.

Accordingly, the band gap energy of each sample became small on the order of the tetragonal $(Bi_{0.97}Ta_{0.03})_2O_{3.06}$, the cubic $(Bi_{0.80}Ta_{0.20})_2O_{3.40}$, and the monoclinic Bi_2O_3 samples, corresponding to the short of the average bond length. Therefore, the optical absorption wavelength of the tetragonal $(Bi_{0.97}Ta_{0.03})_2O_{3.06}$ sample was located on the lowest energy (i.e., longer wavelength) side. The slope of the reflectance spectrum became moderate in the case of the cubic $(Bi_{0.80}Ta_{0.20})_2O_{3.40}$ sample, because of the reduction of the hybrid effect due to the decrease in the Bi^{3+} content. Among the $(Bi_{1-x}Ta_x)_2O_{3+2x}$ samples synthesized in this study, the $(Bi_{0.97}Ta_{0.03})_2O_{3.06}$ sample exhibited the strongest absorption in the green-blue light region (480−490 nm), which is the complementary color of orange.

The UV−vis reflectance spectrum of the $(Bi_{0.97}Ta_{0.03})_2O_{3.06}$ pigment was compared with those for the commercially available orange pigments such as Bayferrox 960 and Bayferrox 4960 (Fe_2O_3−FeOOH, Ozeki Co., Ltd.), as shown in Figure 4.

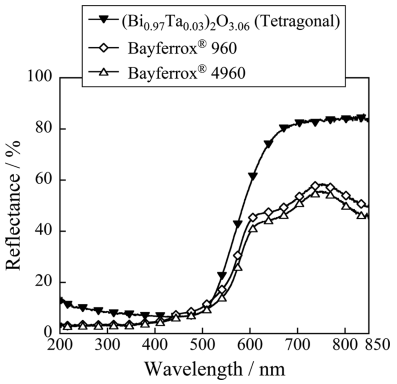

Figure 4. UV−vis reflectance spectra for $(Bi_{0.97}Ta_{0.03})_2O_{3.06}$, Bayferrox 960, and Bayferrox 4960 pigments.

The present $(Bi_{0.97}Ta_{0.03})_2O_{3.06}$ pigment showed higher reflectance in the wavelength region of 580−850 nm corresponding to the yellow-red light as compared with the commercially available orange pigments. But unfortunately, the reflectance in the green light region (520−570 nm) was also higher than those of the commercial ones.

2.3. Chromatic Properties. The $L^*a^*b^*Ch^\circ$ color coordinate data and band gap energies (E_g) for $(Bi_{1-x}Ta_x)_2O_{3+2x}$ (x = 0, 0.03, 0.04, and 0.20) and commercial orange Bayferrox 960 and Bayferrox 4960 pigments are summarized in Table 3. The photographs of these pigments are also displayed in Figure 5. It is obvious that both a^* and b^* values increased in a positive direction by the introduction of Ta^{5+} in the host Bi_2O_3 lattice. Among them, the tetragonal $(Bi_{0.97}Ta_{0.03})_2O_{3.06}$ sample strongly absorbed green and blue (complementary color of orange) lights and exhibited the most vivid orange color with the highest a^* value.

Table 3. $L^*a^*b^*Ch^\circ$ Color Coordinate Data and Band gap Energies (E_g) for $(Bi_{1-x}Ta_x)_2O_{3+2x}$ (x = 0, 0.03, 0.04, and 0.20), Bayferrox 960, and Bayferrox 4960 Pigments

samples	L^*	a^*	b^*	C	h°	E_g/eV
Bi_2O_3	94.0	−9.64	+31.5	32.9	107	2.85
$(Bi_{0.97}Ta_{0.03})_2O_{3.06}$	63.2	+17.3	+56.3	58.9	72.9	2.27
$(Bi_{0.96}Ta_{0.04})_2O_{3.08}$	66.1	+15.2	+60.6	62.5	75.9	2.29
$(Bi_{0.80}Ta_{0.20})_2O_{3.40}$	82.7	+4.70	+46.3	46.5	84.2	2.74
Bayferrox 960	59.0	+21.0	+47.5	51.9	66.1	2.13
Bayferrox 4960	55.9	+23.5	+47.3	52.8	63.6	2.12

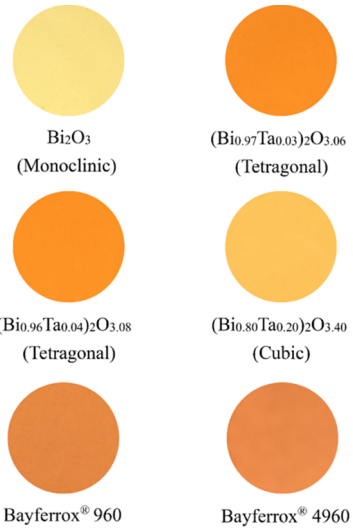

Figure 5. Photographs of the $(Bi_{1-x}Ta_x)_2O_{3+2x}$ (x = 0, 0.03, 0.04, and 0.20), Bayferrox 960, and Bayferrox 4960 pigments.

The color of materials can be affected by a combination of factors, such as particle size, packing density, crystal structure, and chemical composition. As the particle size of the pigment decreases, the color tends to be brighter or lighter.[32] As shown in Figure 2, there was no difference in the particle size of monoclinic Bi_2O_3 and tetragonal $(Bi_{1-x}Ta_x)_2O_{3+x}$ (x = 0.03 and 0.04). Therefore, the color of these pigments depends on the crystal system. In contrast, the particle size of $(Bi_{0.80}Ta_{0.20})_2O_{3.40}$ was smaller than those of other samples and the color of $(Bi_{0.80}Ta_{0.20})_2O_{3.40}$ was relatively light. The pale coloration can be attributed not only to the change of the crystal structure but also the reduction of the particle size.

As seen in Table 3, the redness value (a^*) for the $(Bi_{0.97}Ta_{0.03})_2O_{3.06}$ pigment was slightly small compared to that of the commercial orange pigments. On the other hand, the yellowness value (b^*) was larger than that of the commercially available orange pigments. As a result, it appeared yellowish orange.

2.4. Chemical Stability Test. The chemical stability of the $(Bi_{0.97}Ta_{0.03})_2O_{3.06}$ pigment was also evaluated. The powder sample was dispersed into 4% acetic acid and 4% ammonium bicarbonate aqueous solutions. After leaving them at room temperature for 6 h, the samples were washed with deionized water and ethanol and then dried at room temperature. The color of the samples after the chemical stability test was evaluated using the colorimeter. Unfortunately, slight color degradation was observed after the soaking test, as summarized in Table 4, so it is necessary to cover the surface using an inert substance such as silica to suppress the color degradation.

DOI: 10.1021/acsomega.9b00555
ACS Omega 2019, 4, 7581−7585

Table 4. $L^*a^*b^*Ch^\circ$ Color Coordinates of $(Bi_{0.97}Ta_{0.03})_2O_{3.06}$ before and after the Chemical Stability Test

treatment	L^*	a^*	b^*	C	h°
nontreatment	63.2	+17.3	+56.3	58.9	72.9
4% CH_3COOH	68.3	+13.8	+51.4	53.2	75.0
4% NH_4HCO_3	67.2	+14.6	+50.0	52.1	73.7

3. CONCLUSIONS

$(Bi_{1-x}Ta_x)_2O_{3+2x}$ ($0 \le x \le 0.20$) solid solutions were synthesized by a conventional solid-state reaction method. The crystal structure of the $(Bi_{1-x}Ta_x)_2O_{3+2x}$ (x = 0, 0.03, 0.04, 0.20) samples depended on the composition, and monoclinic α-phase (x = 0), tetragonal β-phase (x = 0.03, 0.04), and cubic δ-phase (x = 0.20) were obtained in a single-phase form. Among these samples, the $(Bi_{0.97}Ta_{0.03})_2O_{3.06}$ pigment strongly absorbed the green-blue light and the band gap energy was 2.27 eV. This pigment presented a vivid yellowish orange color, because the redness value (a^*) of this pigment was slightly smaller and the yellowness value (b^*) was larger than those of commercial orange pigments. Although it is necessary to improve chemical stability, the $(Bi_{0.97}Ta_{0.03})_2O_{3.06}$ pigment has potential to be one of the environmentally friendly inorganic orange pigments.

4. EXPERIMENTAL SECTION

4.1. Materials and Methods. The $(Bi_{1-x}Ta_x)_2O_{3+2x}$ ($0 \le x \le 0.20$) samples were synthesized using a conventional solid-state reaction technique. Stoichiometric amounts of Bi_2O_3 (Kishida Chemical Co., Ltd., 99.9%) and Ta_2O_5 (Wako Pure Chemical Industries, Ltd., 99.9%) were mixed in an agate mortar. The homogenous mixtures were calcined in an aluminum silicate (mullite) crucible at 800 °C for 6 h in air. Finally, the samples were ground in an agate mortar before characterization.

4.2. Characterization. The crystal structures were identified by X-ray powder diffraction (XRD, Rigaku Ultima IV) using Cu Kα radiation (40 kV, 40 mA). The sampling width and scan speed were 0.02 and 6.0° min^{-1}, respectively. The lattice parameters and volumes were calculated from the peak angles, which were refined using α-Al_2O_3 as a standard and using CellCalc Ver. 2.20 software. The sample compositions analyzed using X-ray fluorescence spectroscopy (Rigaku, ZSX Primus) were in good agreement with the nominal stoichiometric compositions of the starting mixtures. The morphology of the $(Bi_{1-x}Ta_x)_2O_{3+2x}$ (x = 0, 0.03, 0.04, and 0.20) particles was investigated by using field-emission-type scanning electron microscopy (FE-SEM; JEOL, JSM-6701F).

The optical reflectance spectra were measured with an ultraviolet−visible (UV−vis) spectrometer (Shimadzu, UV-2550) with barium sulfate as a reference. The band gap energies of the samples were calculated from the absorption edge of the absorbance spectrum represented by the Kubelka−Munk function, $f(R) = (1 - R)^2/2R$, where R is reflectance.[33] The color property was evaluated in terms of the Commission Internationale de l'Éclairage $L^*a^*b^*Ch^\circ$ system using a colorimeter (Konica-Minolta, CR-300). The L^* parameter indicates the brightness or darkness of a color on relation to a neutral gray scale, and the a^* (the red-green axis) and the b^* (the yellow-blue axis) parameters express the color qualitatively. Chroma parameter (C) represents the color saturation of the pigments and is calculated according to the following formula: $C = [(a^*)^2 + (b^*)^2]^{1/2}$. The parameter h° ranges from 0 to 360°, and is calculated with the formula, $h^\circ = \tan^{-1}(b^*/a^*)$.

AUTHOR INFORMATION

Corresponding Author

*E-mail: masui@tottori-u.ac.jp. Phone/Fax: +81−857−31−5264.

ORCID

Toshiyuki Masui: 0000-0002-1755-4603

Notes

The authors declare no competing financial interest.

ACKNOWLEDGMENTS

This work was partially supported by the Grant-in-Aid for JSPS Research Fellow (R.O.).

REFERENCES

(1) Šulcová, P.; Trojan, M. Thermal synthesis and properties of the $(Bi_2O_3)_{1-x}(Ho_2O_3)_x$ pigments. *J. Therm. Anal. Calorim.* **2006**, *83*, 557−559.

(2) Šulcová, P.; Trojan, M. Thermal analysis of pigments based on Bi_2O_3. *J. Therm. Anal. Calorim.* **2006**, *84*, 737−740.

(3) Šulcová, P.; Trojan, M. Thermal synthesis of the $(Bi_2O_3)_{1-x}(Er_2O_3)_x$ pigments. *J. Therm. Anal. Calorim.* **2007**, *88*, 111−113.

(4) Šulcová, P.; Trojan, M. Thermal analysis of the $(Bi_2O_3)_{1-x}(Y_2O_3)_x$ pigments. *J. Therm. Anal. Calorim.* **2008**, *91*, 151−154.

(5) Gonzalvo, B.; Romero, J.; Fernández, F.; Torralvo, M. J. $(Bi,R)_2O_3$ (R: Nd, Sm and Dy) oxides as potential pigments. *J. Alloys Compd.* **2001**, *323*−*324*, 372−375.

(6) Strnadlová, L.; Šulcová, P.; Llusar, M. Thermal study of the $Ce_{0.9}Tb_{0.1}O_2$ pigment prepared by different synthesis. *J. Therm. Anal. Calorim.* **2010**, *102*, 661−665.

(7) Stránská, L.; Šulcová, P.; Vlček, M. Synthesis and properties of inorganic pigments based on pyrochlore compounds with different lanthanides. *J. Therm. Anal. Calorim.* **2013**, *113*, 127−135.

(8) Rao, R. G.; Divya, D. Synthesis and characterization of orange pigments from rare earth metal ions. *Asian J. Chem.* **2017**, *29*, 1673−1676.

(9) Schildhammer, D.; Fuhrmann, G.; Petschnig, L.; Schottenberger, H.; Huppertz, H. Synthesis and optical properties of new highly NIR reflective inorganic pigments $RE_6Mo_2O_{15}$ (*RE* = Tb, Dy, Ho, Er). *Dyes Pigm.* **2017**, *140*, 22−28.

(10) Bae, B.; Takeuchi, N.; Tamura, S.; Imanaka, N. Environmentally friendly orange pigments based on hexagonal perovskite-type compounds and their high NIR reflectivity. *Dyes Pigm.* **2017**, *147*, 523−528.

(11) Bradley, B.; Singleton, M.; Li Wan Po, A. Bismuth toxicity − A reassessment. *J. Clin. Pharm. Ther.* **1989**, *14*, 423−441.

(12) Winship, K. A. Toxicity of bismuth salts. *Adverse Drug React. Acute Poisoning Rev.* **1983**, *2*, 103−121.

(13) Serfontein, W. J.; Mekel, R. Bismuth toxicity in man. II. Review of bismuth blood and urine levels in patients after administration of therapeutic bismuth formulations in relation to the problem of bismuth toxicity in man. *Res. Commun. Chem. Pathol. Pharmacol.* **1979**, *26*, 391−411.

(14) Sammes, N. M.; Tompsett, G. A.; Näfe, H.; Aldinger, F. Bismuth based oxide electrolytes - structure and ionic conductivity. *J. Eur. Ceram. Soc.* **1999**, *19*, 1801−1826.

(15) Zhang, L.; Wang, W.; Yang, J.; Chen, Z.; Zhang, W.; Zhou, L.; Liu, S. Sonochemical synthesis of nanocrystallite Bi_2O_3 as a visible-light-driven photocatalyst. *Appl. Catal., A* **2006**, *308*, 105−110.

DOI: 10.1021/acsomega.9b00555
ACS Omega 2019, 4, 7581−7585

(16) Cheng, H.; Huang, B.; Lu, J.; Wang, Z.; Xu, B.; Qin, X.; Zhang, X.; Dai, Y. Synergistic effect of crystal and electronic structures on the visible-light-driven photocatalytic performances of Bi_2O_3 polymorphs. *Phys. Chem. Chem. Phys.* **2010**, *12*, 15468−15475.
(17) Wang, F.; Cao, K.; Zhang, Q.; Gong, X.; Zhou, Y. A computational study on the photoelectric properties of various Bi_2O_3 polymorphs as visible-light driven photocatalysts. *J. Mol. Model.* **2014**, *20*, No. 2506.
(18) Li, Q.-Y.; Zhao, Z.-Y. Interfacial properties of α/β-Bi_2O_3 homojunction from first-principles caluculations. *Phys. Lett. A* **2015**, *379*, 2766−2771.
(19) Li, L.; Meng, L.; Wang, F.; Wang, Y. Synthesis and optical characterization of In^{3+}-stabilized γ-Bi_2O_3 sillenite semiconductor with cation deficiency. *Mater. Sci. Semicond. Process.* **2017**, *68*, 48−52.
(20) Takahashi, T.; Iwahara, H.; Esaka, T. High oxide ion conduction in sintered oxide of the system Bi_2O_3-M_2O_5. *J. Electrochem. Soc.* **1977**, *124*, 1563−1569.
(21) Takahashi, T.; Iwahara, H. Oxide ion conductors based on bismuthsesquioxide. *Mater. Res. Bull.* **1978**, *13*, 1447−1453.
(22) Iwahara, H.; Esaka, T.; Sato, T.; Takahashi, T. Formation of high oxide ion conductive phases in the sintered oxides of the system Bi_2O_3-Ln_2O_3 (*Ln* = La-Yb). *J. Solid State Chem.* **1981**, *39*, 173−180.
(23) Ahila, M.; Subramanian, E.; Pathinettam, P. D. Optical properties of *Codium tomentosum* seaweed like Bi_2O_3 nanostructure and its gas-sensing activity. *Ionics* **2018**, *24*, 1827−1839.
(24) Manjula, M.; Karthikeyan, B.; Sastikumar, D. Sensing characteristics of clad-modified (Ho-doped Bi_2O_3 nanoparticles) fibre optic gas sensor. *Opt. Fiber Technol.* **2018**, *45*, 35−39.
(25) Blower, S. K.; Greaves, C. The structure of β-Bi_2O_3 from powder neutron diffraction data. *Acta Crystallogr., Sect. C: Cryst. Struct. Commun.* **1988**, *44*, 587−589.
(26) Kusumoto, K. Synthesis of Bi_2O_3−Nb_2O_5 solid solutions for environmental-friendly reddish yellow pigments. *J. Ceram. Soc. Jpn.* **2016**, *124*, 926−928.
(27) Hull, S.; Norberg, S. T.; Tucker, M. G.; Eriksson, S. G.; Mohn, C. E.; Stølen, S. Neutron total scattering study of the δ and β phases of Bi_2O_3. *Dalton Trans.* **2009**, 8737−8745.
(28) Shannon, R. D. Revised effective ionic radii and systematic studies of interatomic distances in halides and chalcogenides. *Acta Crystallogr., Sect. A: Cryst. Phys., Diffr., Theor. Gen. Crystallogr.* **1976**, *32*, 751−767.
(29) Evarestov, R. A.; Shapovalov, V. O.; Veryazov, V. A. Electronic structure and chemical bonding in Bi_2O_3. *Phys. Status Solidi B* **1994**, *183*, K15−K17.
(30) Wendusu; Ikawa, K.; Masui, T.; Imanaka, N. Novel environment-friendly yellow pigments based on (Bi, La)VO_4. *Chem. Lett.* **2011**, *40*, 792−794.
(31) Masui, T.; Honda, T.; Wendusu; Imanaka, N. Novel and environmentally friendly (Bi,Ca,Zn)VO_4 yellow pigments. *Dyes Pigm.* **2013**, *99*, 636−641.
(32) Ke, S.; Wang, Y.; Pan, Z. Effects of precipitant and surfactant on co-precipitation synthesis of $Nd_2Si_2O_7$ ceramic pigment. *Dyes Pigm.* **2015**, *118*, 145−151.
(33) Kubelka, P.; Munk, F. An article on optics of paint layers. *Z. Tech. Phys.* **1931**, *12*, 593−601.

DOI: 10.1021/acsomega.9b00555
ACS Omega 2019, 4, 7581−7585